

©Copyright 2019

M. P. Ross

Development and Deployment of Precision Mechanical Rotation Sensor for Terrestrial Gravitational Wave Observatories

M. P. Ross

A dissertation
submitted in partial fulfillment of the
requirements for the degree of

Doctor of Philosophy

University of Washington

2019

Reading Committee:

Name of Chairperson, Chair

First committee member

Next committee member

etc

Program Authorized to Offer Degree:
Physics

University of Washington

Abstract

Development and Deployment of Precision Mechanical Rotation Sensor for Terrestrial
Gravitational Wave Observatories

M. P. Ross

Chair of the Supervisory Committee:
Title of Chair Name of Chairperson
Department of Chair

TABLE OF CONTENTS

	Page
List of Figures	iii
Chapter 1: Introduction	1
1.1 Gravitational Wave Theory	1
1.2 LIGO	1
1.3 Seismic Isolation	1
Chapter 2: 1-m Scale Ground Rotation Sensors	2
2.1 Tilt Contamination	2
2.2 Sensor Correction with Tilt Subtraction	4
2.3 Mechanical System	5
2.4 Multi-Slit Autocollimator Readout	5
2.5 Controls	8
2.6 Noise Performance	9
2.7 Hanford Installation	9
2.8 Livingston Installation	12
Chapter 3: 30-cm Scale On-Board Rotation Sensors	13
3.1 Angular Controls	13
3.2 Isolation Scheme	14
3.3 Mechanical System	14
3.4 Interferometric Readout	14
3.5 Mass Adjustment	16
3.6 Controls	17
3.7 Noise Performance	17

Chapter 4:	Applications	18
4.1	Geophysics	18
4.1.1	Rayleigh Wave Theory	18
4.1.2	Wave Field Parameter Extraction	19
4.1.3	Single Station Dispersion Measurements	20
4.2	Newtonian Noise	22
4.2.1	Theory	22
4.2.2	Observations	22

LIST OF FIGURES

Figure Number	Page
2.1	3
2.2	6
2.3	10
2.4	11
2.5	11
3.1	15
3.2	15
4.1 cite tilt seismology	21
4.2	22

DEDICATION

To Grace

Chapter 1

INTRODUCTION

1.1 Gravitational Wave Theory

1.2 LIGO

1.3 Seismic Isolation

Chapter 2

1-M SCALE GROUND ROTATION SENSORS

2.1 *Tilt Contamination*

At their core seismometers are low frequency spring mass system which measures the difference in motion between the casing and the device's proof mass. Above the resonant frequency of the spring mass system, this allows for accurate measurements of the motion in reference to an inertial frame of any object that the casing is rigidly connected to, be it the ground or a suspended table. Over the past **some time** this technology has produced devices that are sensitive to **number and range**. However, these systems are fundamentally susceptible to any stray forces acting on the proof mass.

Of interest here is the contamination due to the rotation of the device within a external gravitational field, namely the field caused by the earth. The rotation in respect to a fixed gravitational force will be referred to as tilt.¹ From the proof mass's frame, a tilt is equivalent to a rotation of the gravitational force. This yields a horizontal acceleration of the proof mass of:

$$a = g \sin(\theta)$$

where g is the gravitational acceleration on the surface of the earth and θ is the angle that the device is rotated. This acceleration adds a second term to the seismometer's output shown below for small angles and in the Fourier domain:

$$\tilde{x}_{seis}(\omega) = \tilde{x}_{trans}(\omega) + \frac{g}{\omega^2} \tilde{\theta}_{wind}(\omega)$$

¹Although a subtle difference, the distinction would be of great consequences if the local gravitational field was varying rapidly. In that case the sensors described here would be of little use as they are rotational sensors not tilt sensors.

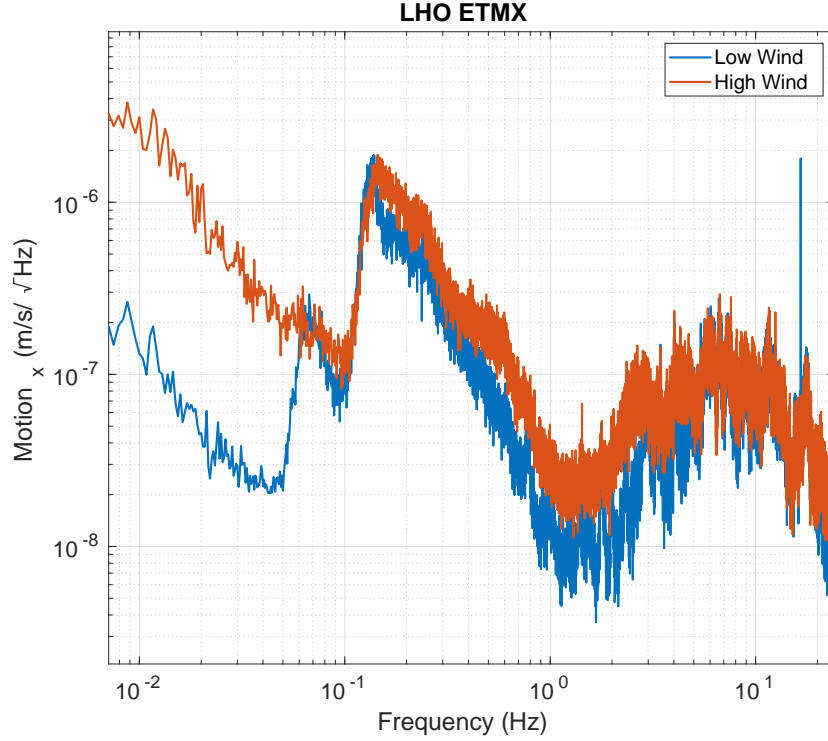


Figure 2.1

where x_{seis} is the seismometer's output, x_{trans} is the translational motion of the device, and ω is the frequency at which the tilt is being driven.

With this additional contribution, it becomes immediately clear that, for a given amplitude of tilt, the contamination term contributes more at lower frequencies and readily dominates the translational signal. In the context of the ground seismometers at the observatory, the tilt signal swamps the translational component below ~ 100 mHz. Above which the seismometer signal is dominated by the ever present oceanic microseism which is driven by low frequency pressure waves with the ocean and their interaction with the shoreline. **CITE** This can be seen in Figure 2.1 which shows an amplitude spectral density of a ground seismometer at LHO during both low and high wind conditions.

The dominant driver of ground tilts at the observatories is wind acting on the walls of

the building. Although one would naiively assume that the wind would rigidly rotate the building, it was found that the true mechanism is differential pressure acting on the walls deforms the building's concrete slab. **cite?**

2.2 Sensor Correction with Tilt Subtraction

There are a few different ways to combat such a contamination. The most straight forward is to decrease the wind pressure by designing builds that don't interact with the wind as much or installing wind blocks such as wind fences or earth burms. Both of these option require significant construction and for the case of LIGO, tilt contamination was not known to be a problem when design the observatories. Another option is to build seismometers that are suspended in such a way that they do not experience tilts. This is an active area of research and may yield tilt-free seismometers. **cite**

The scheme that will be used here is to measure the tilt with an independent rotation sensor and subtract the wind driven contribution. This would then yield a channel of the following form:

$$x_{seis}(\omega) = x_{trans}(\omega) + \frac{g}{\omega^2} \theta_{wind}(\omega) \quad (2.1)$$

$$- \frac{g}{\omega^2} \theta_{meas}(\omega) \quad (2.2)$$

where θ_{meas} is the tilt seen by the rotation sensor. Given a coherence γ between the tilt component of the seismometer and rotation sensors this yields the following: **CHECK math**

$$x_{seis}(\omega) = x_{trans}(\omega) + \frac{g}{\omega^2} (1 - \gamma) \theta_{wind}(\omega)$$

This is then a low tilt channel which can be used within the LIGO seismic isolation system.

2.3 Mechanical System

The Beam Rotation Sensor (BRS) is a beam balance comprised of a 1-m long beam hung from two 10-15 μm thick beryllium-copper flexures. Figure 2.2 shows a CAD model of the beam balance.

This design makes the beam stiff in all degrees of freedom other than rotations around the horizontal axis which intersects the two flexure pivot points. This forms a system consisting of two elementary subsystems: a rotational spring mass system formed by the stiffness of the flexures, and a simple pendulum due to the offset of the pivot point and the center of mass. This is then described by the following equation of motion: [17]

$$I\ddot{\theta}(t) + \kappa(1 + \frac{i}{Q})(\theta(t) - \theta_p(t)) + Mg\delta\theta(t) + M\delta\ddot{x}_p(t) = \tau_{ex}(t)$$

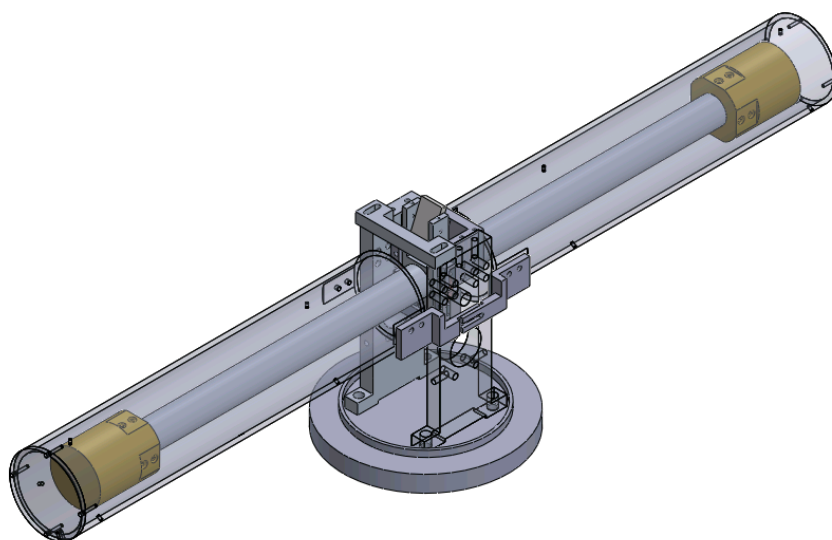
where θ and θ_p are, respectively, the angle of beam and the platform with respect to gravitational vertical, τ_{ext} is the sum of all exterior torques, I is the moment of inertia, Q is the quality factor of the system, κ is the spring constant of the flexures, M is the mass of the balance, g is the gravitational acceleration, δ is the vertical distance from the center of mass and the pivot point, and x_p is the translation of the platform.

derive translational coupling and readout equation

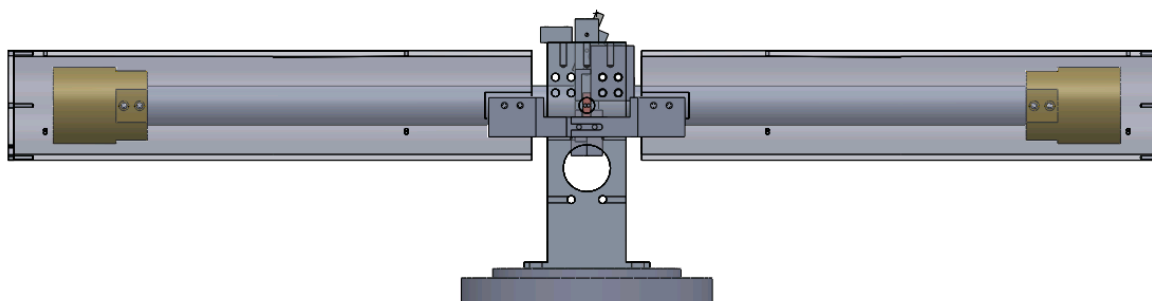
In ideal operation, one would tune the center of mass to be at the pivot point and thus would produce a pure rotational spring-mass system with no translational coupling. In this limit, the rotation sensor is a rotational analog to a seismometer; above the resonant frequency as the casing rotates the beam stays inertial and thus allows one to measure the casing's rotation.

2.4 Multi-Slit Autocollimator Readout

Optical levers are a simple optical angular readout which exploits the law of reflection to measure angular deflections of a mirror by observing the displacement of a reflected beam.



(a)



The angle of the mirror is then described as:

$$\theta_{mirror} = \frac{x_{reflected}}{2d}$$

where θ_{mirror} is the angle of the mirror, $x_{reflected}$ is the displacement of the reflected beam, and d is the distance between the optical system and the mirror. This allows one to increase the precision of the angular measurements arbitrarily by increasing d . However, with this comes a few disadvantages. One the effective gain of the sensor depends of the d which may not be well known. Additionally, the system is sensitive to changes in d .

An autocollimator adds a lens located one focal length from light source and the screen, shown in Figure **number**. This effectively replace the distance dependence with the focal length of the lens which allows the system to be only sensitive, to first order, to the angular motion of the mirror.

autocollimator schematic

To improve upon this further, a partially reflective mirror can be placed in between the optical system and the main mirror to act as a reference and allows for the subtraction of any motion of the optical system with respect to the main mirror. This yield a angular readout described by:

$$\theta_{mirror} = \frac{x_{main} - x_{reference}}{2f}$$

where f is the focal length of the lens and $x_{reference}$ is the beam spot from the reference mirror.

make table of BRS autocollimator parameters: focus, number of slits, slit width, CCD type, light source, frequency

An increase in sensitivity can be made by employing a multi-slit autocollimator [2]. This consists of an autocollimator with the light source replaced by a illuminated photomask of a number of thin slits. The pattern is then reflected off a set of reference and main mirror and imaged by a line CCD camera. These images are then analyzed to measure the distance between them thus yielding a measurement of angle. For the BRSs, this

image analysis is achieved using bespoke software written in C# which can be found at www.github.com/mpross/BRSReadout

To extract the distance between the patterns, the image goes through a series of steps to go from a vector of pixel intensities to a single angular output. When the software begins, the first frame that is captured is saved. All future frames are split into two, with one part representing the reference mirror and the other the main mirror. The cross correlation is then taken between each part and it's matching part from the first frame. This gives a curve who's maximum is located at the pixel number corresponding to separation between the pattern in the current frame and the first frame, which can be seen in Figure **number**. The points of this curve that are near the maximum are then fit to a Gaussian which allows for the extraction of the location of the peak with sub-pixel resolution. This is done for each pattern separately after which the difference between the reference pattern location and the main pattern location is taken. The difference is then proportional to the change in angle between the casing and the beam.

Compared to previous image analysis algorithms [?], this algorithm is more computationally efficient while also being less susceptible to variations in the pattern image due to dust particulate, incorrect focusing, or beam clipping. A sensitivity of $\sim 0.1 \text{ nrad}/\sqrt{\text{Hz}}$ was achieved with this autocollimator design and image analysis algorithm.

2.5 Controls

As the BRSs are installed in active lab spaces, anthropogenic actively and environmental disturbances regularly apply torques on the beam balance, either through mechanical coupling through the flexures or gravitational coupling with the end masses. These can then cause the motion at the resonant frequency to rise to undesirable amplitudes. As the beam motion increases so does the noise. Additionally, some disturbances can be large enough to cause the amplitude to exceed the dynamic range of the autocollimator readout system.

To alleviate this issue, capacitor plates are installed underneath each end of the beam

balance to act as actuators. The force between the two capacitor plates follows the following:

$$F = \frac{\epsilon AV^2}{2d^2}$$

where ϵ is the permittivity of the material between the plates, A is the area of the plate, V is the voltage applied to the plates, and d is the distance between the plates. The plate under the beam is connected to a DAC while the beam is grounded which allows for a controlled actuation torque to be applied to the beam.

The control scheme that was adopted was one in which the feedback signal that is sent to the capacitors is the angular velocity of the beam band passed between 2 mHz and 20 mHz to include only motion at frequencies near the resonance. The feedback is additionally applied with low gain so that the feedback is only adding loss to the system as compared to locking the system in a strong feedback loop where all of the motion is absorbed into the control system. This is then implemented with two gain stages, a “low amplitude” stage which is always on and yields a Q of 10-15 and a “high amplitude” stage which is triggered if the amplitude rises above a threshold that is set based on the behavior of the given device and gives a Q of **number**.

2.6 Noise Performance

2.7 Hanford Installation

Between the first (O1) and second (O2) observing runs of LIGO, two BRSs were installed at the LIGO Hanford Observatory, one at each end station correcting the translations along their respective arm. Although one would expect that the corner station sensors would also need to be corrected, a location was found within the corner station building which exhibited low tilt. **cite** This is thought to be due to the shape of the building the distance between this location and the walls. As such no BRS was necessary to achieve low tilt injection seismic isolation.

The tilt subtraction performance achieved with these devices can be seen in Figure 2.3

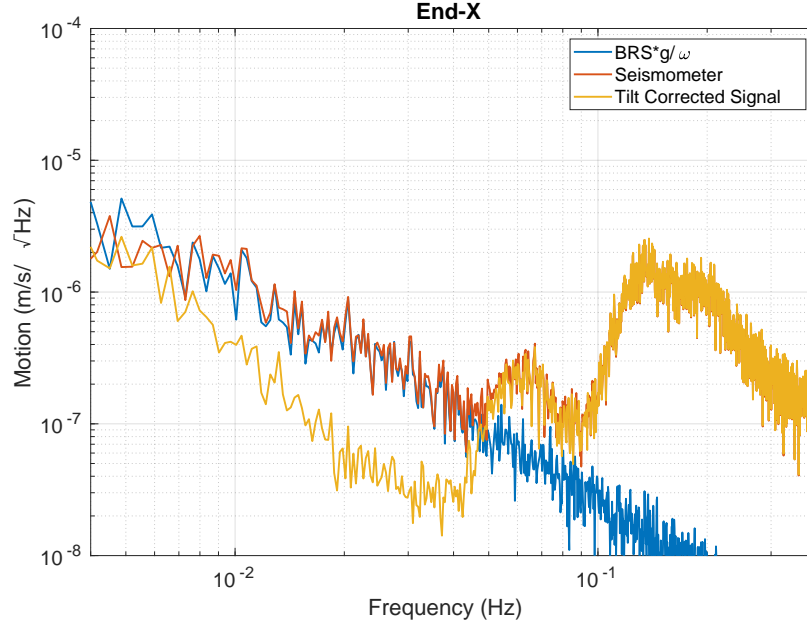


Figure 2.3

where it is evident that the system achieves tilt subtraction from around 6 mHz to 50 mHz. Above 50 mHz the seismometer signal is dominated by the oceanic microseism and the tilt contribution is negligible. Below 6 mHz, the BRS signal becomes overwhelmed by instrumental noise. This performance can also be seen in Figure 2.4 which shows a example time series of the tilt subtraction.

This tilt subtracted channel was then used as the ground signal for the isolation's sensor correction instead of the raw seismometer. Along with the use of the low tilt seismometer for the corner station, the addition of the BRSs in the seismic control scheme yielded significant improvements in the ability to lock the interferometer at increased wind speeds which can be seen in Figure 2.5

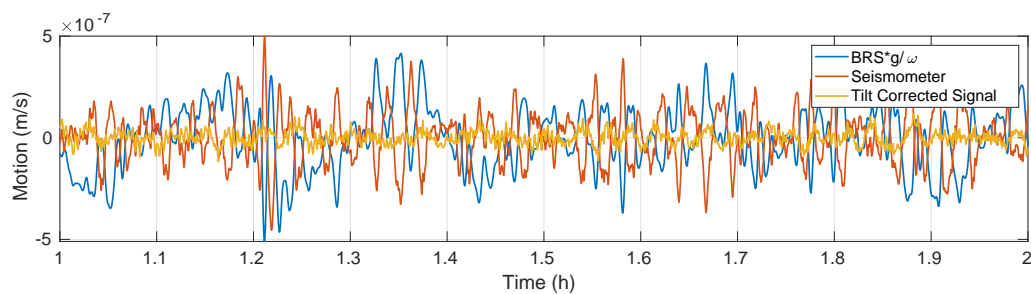


Figure 2.4

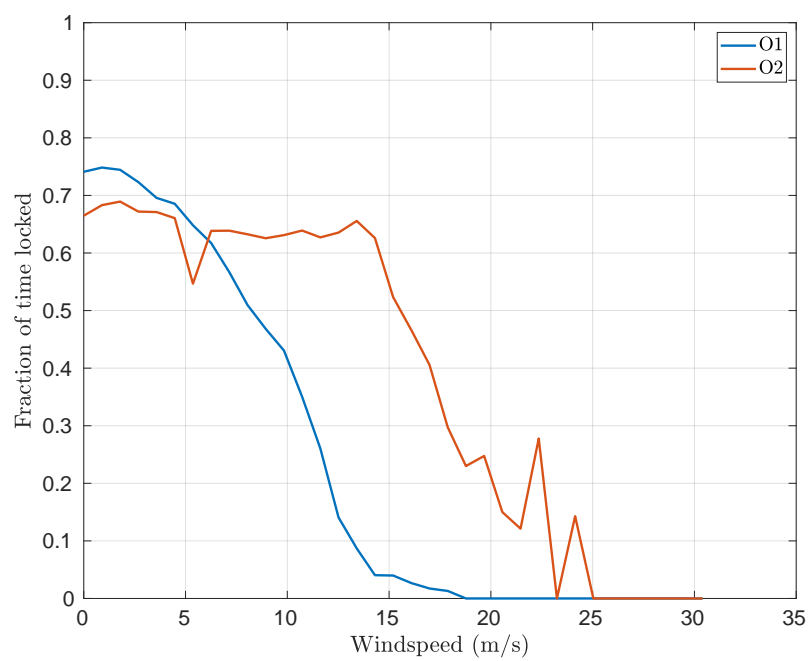


Figure 2.5

2.8 *Livingston Installation*

After the success of the Hanford BRS installation, four devices were installed at the LIGO Livingston Observatory (LLO) between the second and third (O3) observing runs. Due to differences in the size and shape of the corner station building at LLO a low tilt location was not found. Thus two BRSs were installed located near the two input test masses (ITM) correcting the seismometer signal oriented along their respective arms.

All four were implemented in a similar fashion as the Hanford devices.

Chapter 3

30-CM SCALE ON-BOARD ROTATION SENSORS

3.1 *Angular Controls*

To operate the LIGO interferometers in their optimal configuration, the angular motion of the test masses in the pitch degree of freedom must be under **number** nrad/ $\sqrt{\text{Hz}}$ at **number** Hz where as the ground rotates at \sim **number** nrad/ $\sqrt{\text{Hz}}$ at **number** Hz. To achieve this desired performance, the seismic isolation operated in the rotational degrees of freedom as well as the translation. Additionally, the upper three masses of the quadruple pendulum are actively actuated at frequencies between **number** and **number** Hz to decrease any residual motion.

With the current system, at **number** Hz the seismic isolation is limited by the sensor noise in the seismometer pair which forms the pitch sensor. This then requires high gain feedback loops on the angular control loop downstream, which themselves are limited by their respective sensor noise at **number** Hz. This left over noise then leaks into the gravitational wave band between **number** and **number** Hz due to the inability to sharply roll off the control without interfering with control at lower frequencies.

add angular controls plot

The compact Beam Rotation Sensor (cBRS), described in the following, was designed to be an alternative angular sensor for the seismic isolation system with **number** times lower noise than the current sensors. With this decreased noise, the seismic isolation control loops can be tuned to significantly increase the performance of both the translational isolation, through decreased tilt contamination described in Section ??, and directly the rotational isolation. Details of this follow in Section 3.2. This decreased residual rotation would then allow the angular control loops to be retuned, specifically decreasing the gain, to push the

sensor noise leakage below the design sensitivity. **Need to check this.**

show noise plot

3.2 Isolation Scheme

Assuming that the isolation is limited by the noise of the in-band sensor, placing the lowest noise sensors on the second stage of the ISI would be expected to yield the lowest angular motion seen by the down stream control loops. With this in mind and the fact that the access to place new sensors is easier for the second stage, a control scheme was modeled which consists of the addition of an idealized cBRS (described in Section ??) on stage 2. This model consisted of only two mechanical degrees of freedom, one horizontal translation and the rotational about the orthogonal horizontal axis.

The rotational control loop for stage 2 then consists of using the CPS between stage 1 and stage 2 at low frequencies, the cBRS at frequencies between 3 mHz and 0.9 Hz, and the GS-13 pairs at frequencies above that. The blend frequencies were tuned to minimized the rms motion at low frequencies while maximizing the isolation at 0.1 Hz.

3.3 Mechanical System

Similar to the BRS described in Chapter 2, the compact Beam Rotation Sensor (cBRS), shown in Figure ??, consists of a 30-cm long cross hung from 10-15 μm thick beryllium-copper flexures and has an identical operating principle as the BRS. The cross shape of the balance decreases the sensitivity of the device to gradients in the local gravitational field while allowing for increased moment of inertia compared to a similarly sized beam.

This design yields a resonant frequency of ~ 20 mHz limited the use of such a device to frequencies above this.

3.4 Interferometric Readout

In order to maintain the small size of the entire device, an interferometric readout was developed that consists of a Fabry-Perot cavity that is formed by a beamsplitter coated

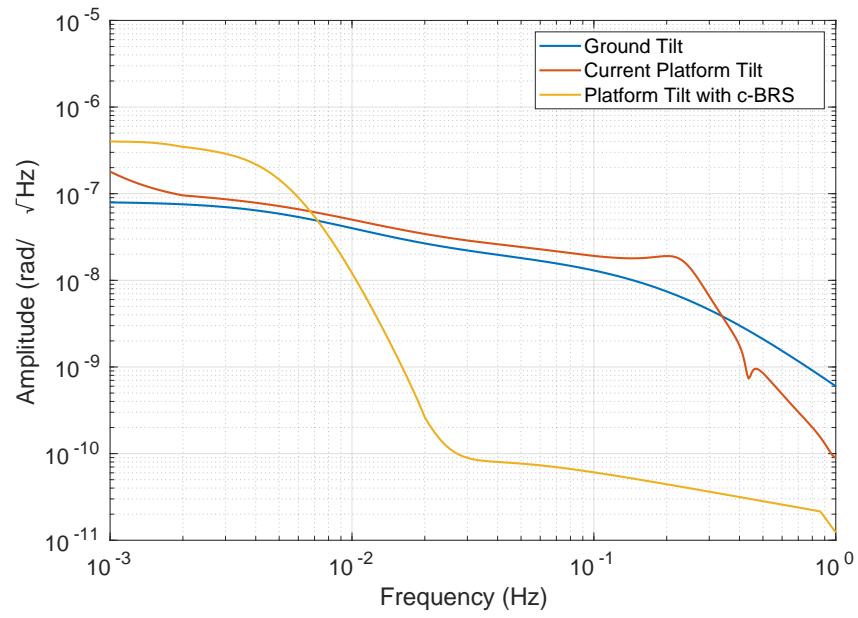


Figure 3.1

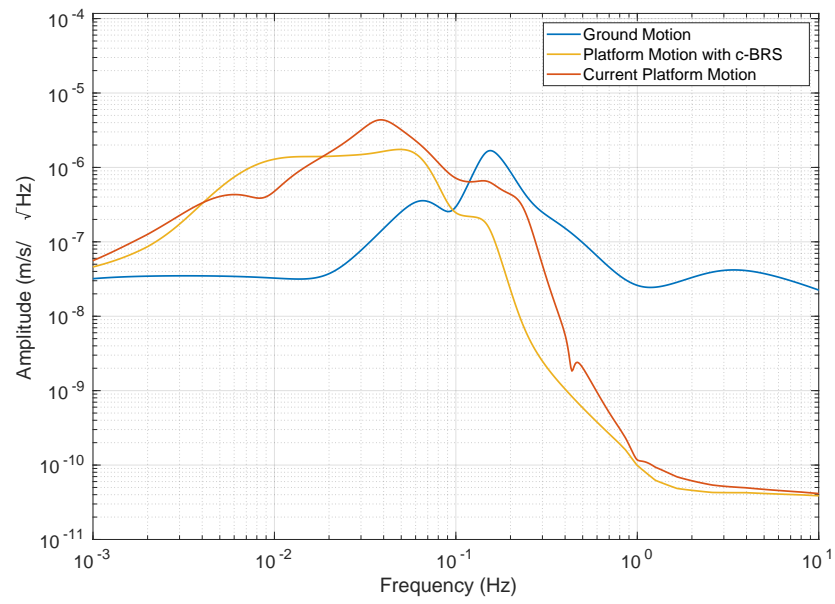
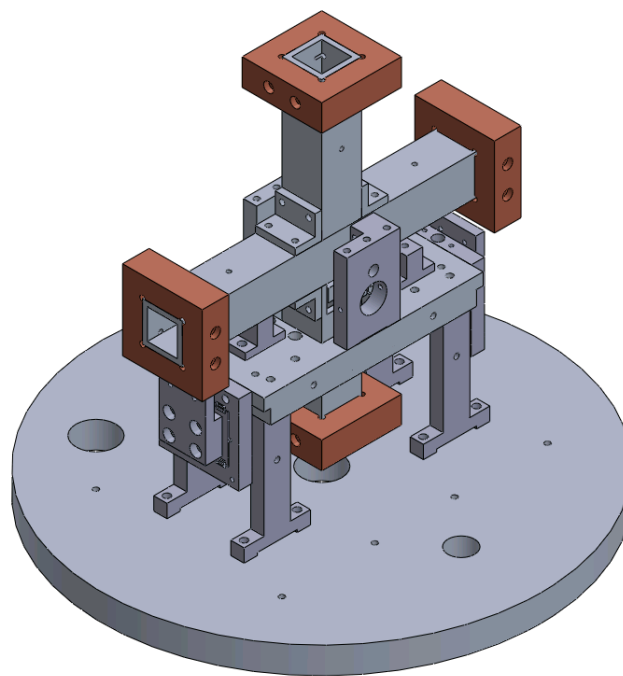
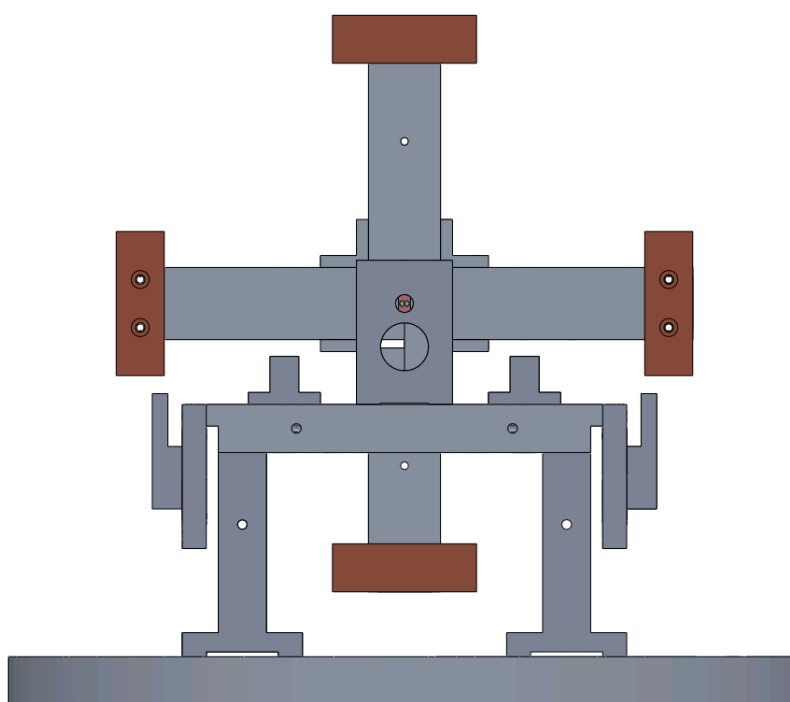


Figure 3.2



(a)



(b)

optical fiber and the full reflectance mirror placed on the bottom of the balance's end masses. The reflectance of this cavity is then monitored by employing a circulator to separate the incoming and outgoing rays. As the cavity length changes the reflectance undergoes an interference pattern described by:

$$\text{someequation} \tag{3.1}$$

include layout of cBRS optics

To linearize this readout, the optical fiber tip and collimating lens are placed on a translation stage that is driven by a piezo stack. The intensity of the reflected light is then fed back to the piezos using a PID loop to hold the cavity length fixed. This allows the system to be separated into two linear readouts, the interferometer output for small ranges above the unity gain frequency (UGF) of the loop and the control loop output for larger motions below the UGF. The output of the device is then the sum of these two channels.

include table of PID parameters

include image of readout noise

3.5 Mass Adjustment

Through a variety of mechanisms, the devices described here can undergo long term drifts of the equilibrium position that can drive the beam balance past the dynamic range of the readout. To counteract this, a mass on the balance can be moved or added to shift the center of mass as such:

$$\Delta\theta = \frac{g}{\kappa}mr \tag{3.2}$$

where $\Delta\theta$ is the change in equilibrium angle, g is the gravitational acceleration, κ is the spring constant of the flexure, m is the mass added, and r is the distance from the mass and the pivot point.

While for the BRS the horizontal center of mass (COM) was designed to be tuned by hand, for the cBRS to operate in vacuum this must be done remotely.

3.6 *Controls*

3.7 *Noise Performance*

Chapter 4

APPLICATIONS

The development of these highly sensitive rotation sensors have opened up a few novel scientific avenues that have been explored and many that have not.

4.1 *Geophysics*

Seismic waves have six components, three translations and three rotations, however seismology has long neglected the rotational components due the lack of sensitive rotation sensors. Recent developments have begun to alleviated this issue with the advent of seismically relevant ring laser gyros. **cite Gryo** The BRSs described above join a small class of ground rotation sensors with high enough sensitivity at low frequency to allow for the use in seismology.

4.1.1 *Rayleigh Wave Theory*

Seismic waves can be broken into two classes: body waves and surface waves. In regard to surface waves there are two polarization, of the motion caused by a Love wave is constrained to the plane parallel with the surface of the medium while Rayleigh waves are constrained to a plane perpendicular the surface.

The plane wave solution of a Rayleigh wave has six components $(u_x, u_y, u_z, \theta_x, \theta_y, \theta_z)$ where u_i designated the translational motion in the i th direction while θ_i is the rotation

about the i th axis. These can be described as with the following **cite seismic paper**

$$u_x(\mathbf{r}, t) = \alpha \sin(\zeta) \cos(\psi) \cos(\omega t - \mathbf{k} \cdot \mathbf{r}) \quad (4.1)$$

$$u_y(\mathbf{r}, t) = \alpha \sin(\zeta) \sin(\psi) \cos(\omega t - \mathbf{k} \cdot \mathbf{r}) \quad (4.2)$$

$$u_z(\mathbf{r}, t) = \alpha \cos(\zeta) \cos(\omega t - \mathbf{k} \cdot \mathbf{r} + \pi/2) \quad (4.3)$$

$$\theta_x(\mathbf{r}, t) = \frac{\partial u_z}{\partial y} = \alpha \kappa \cos(\zeta) \sin(\psi) \cos(\omega t - \mathbf{k} \cdot \mathbf{r}) \quad (4.4)$$

$$\theta_y(\mathbf{r}, t) = -\frac{\partial u_z}{\partial x} = -\alpha \kappa \cos(\zeta) \cos(\psi) \cos(\omega t - \mathbf{k} \cdot \mathbf{r}) \quad (4.5)$$

$$\theta_z(\mathbf{r}, t) = \frac{1}{2} \left(\frac{\partial u_y}{\partial x} - \frac{\partial u_x}{\partial y} \right) = 0 \quad (4.6)$$

where α is the amplitude, ζ is the ellipticity angle, ψ is the angle of incidence in the horizontal plane, ω is the frequency, and $\mathbf{k} = \kappa(\cos(\psi), \sin(\psi), 0)$ is the wavevector.

From these equations it can be seen that with a single seismic station with a traditional 3-axis seismometer, one can not measure all five parameters that define this wave field. Additionally, the horizontal components, u_x and u_y can contain contributions from co-propagating Love waves which further muddles ones ability to extract parameters.

4.1.2 Wave Field Parameter Extraction

With the combined measurements of the translational and rotational components at a single station, one can readily extract wavefield parameters that would otherwise be difficult to obtain, namely the phase velocity and the angle of incidence.

Seismic wave phase velocities are common observable which not only allows for understanding of Rayleigh wave propagation but can be inverted to yield tomographical structure profiles of the interior of the earth. **cite** The traditional method of extracting these is the exploit the time of arrival of a wave as it passes through an array of many seismometers. The analysis can be constrained to only the vertical channel which is insensitive to Love waves which could contaminate the measurements. However, this method requires many devices

and effectively averages over the size of the array.

Alternatively, with measurements of the rotational components a point like measurement of the phase velocity can be made with three devices, a 3-component seismometer and two horizontal rotation sensors. This can be shown in the following equations:

$$v = \frac{\omega}{\kappa} = \frac{\dot{u}_z}{\theta_x} \sin(\psi) \quad (4.7)$$

$$v = \frac{\dot{u}_z}{\theta_y} \cos(\psi) \quad (4.8)$$

$$v = \frac{\dot{u}_z}{\sqrt{\theta_x^2 + \theta_y^2}} \quad (4.9)$$

where the dot represents the temporal derivative. Equations 4.7 and 4.8 can be utilized if a station has only one horizontal rotation sensor but requires independent determination of ψ . In contrast, Equation 4.9 contains only information from a single station.

In addition to the phase velocity, the angle of incidence can be determined with the following:

$$\psi = \arctan\left(\frac{\theta_x}{\theta_y}\right) \quad (4.10)$$

Although in theory, this can be measured using a single seismometer, Love wave contamination of the horizontal translational channels would distort any such measurement. As the horizontal rotational channels are insensitive to Love waves, they allow the extraction of ψ without such contamination.

4.1.3 Single Station Dispersion Measurements

Hanford Measurements

As described in Section 2.7, two BRSs were installed at LHO, one at each end station located 5.66 meters apart.

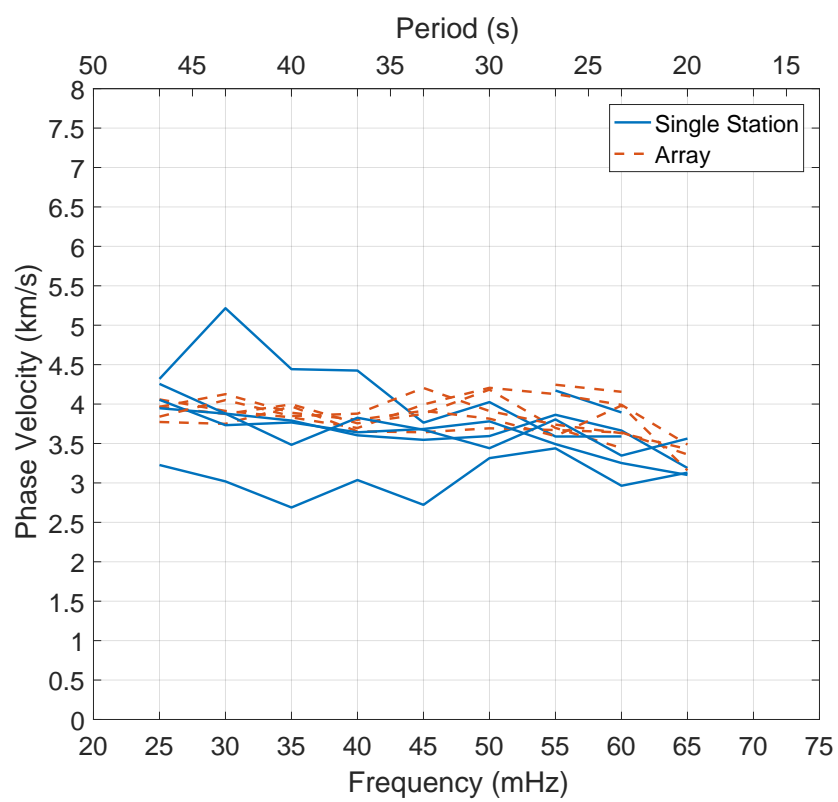


Figure 4.1: cite tilt seismology

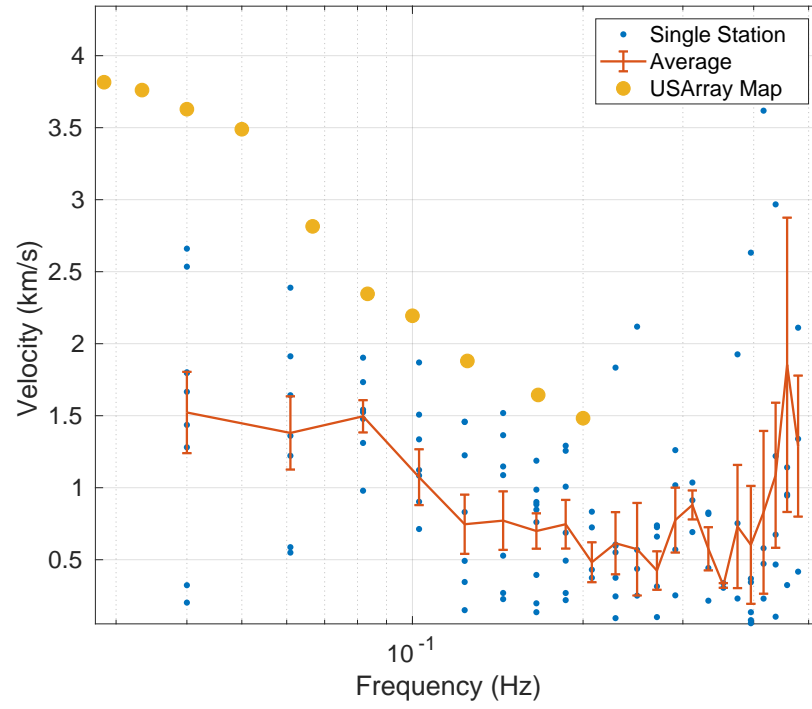


Figure 4.2

Livingston Measurements

4.2 Newtonian Noise

4.2.1 Theory

4.2.2 Observations

BIBLIOGRAPHY

- [1] Aasi, J. et al. (2015). Advanced ligo. *Classical and Quantum Gravity*, 32(7):074001.
- [2] B Arp, T., A Hagedorn, C., Schlamming, S., and H Gundlach, J. (2013). A reference-beam autocollimator with nanoradian sensitivity from mhz to khz and dynamic range of 10(7.). *The Review of scientific instruments*, 84:095007.
- [3] Belfi, J., Beverini, N., Carelli, G., Di Virgilio, A., Maccioni, E., Saccorotti, G., Stefani, F., and Velikoseltsev, A. (2012). Horizontal rotation signals detected by “g-pisa” ring laser for the mw = 9.0, march 2011, japan earthquake. *Journal of Seismology*, 16(4):767–776.
- [4] et. al., S. (2016). First deep underground observation of rotational signals from an earthquake at teleseismic distance using a large ring laser gyroscope. *arXiv*.
- [5] Haskell, N. A. (1953). The dispersion of surface waves on multilayered media. *Bulletin of the Seismological Society of America*, 43(1):17–34.
- [6] Lantz, B., Schofield, R., O’Reilly, B., Clark, D. E., and DeBra, D. (2009). Review: Requirements for a ground rotation sensor to improve advanced ligo. *Bulletin of the Seismological Society of America*, 99(2B):980–989.
- [7] Lee, W. H. K., Celebi, M., Todorovska, M. I., and Igel, H. (2009). Introduction to the special issue on rotational seismology and engineering applications. *Bulletin of the Seismological Society of America*, 99(2B):945–957.
- [8] Legendre, C. P., Zhao, L., Huang, W.-G., and Huang, B.-S. (2015). Anisotropic rayleigh-wave phase velocities beneath northern vietnam. *Earth, Planets and Space*, 67(1):28.

- [9] Lin, C.-J., Huang, H.-P., Pham, N. D., Liu, C.-C., Chi, W.-C., and Lee, W. H. K. (2011). Rotational motions for teleseismic surface waves. *Geophysical Research Letters*, 38(15):n/a–n/a. L15301.
- [10] Lin, F.-C., Moschetti, M. P., and Ritzwoller, M. H. (2008). Surface wave tomography of the western united states from ambient seismic noise: Rayleigh and love wave phase velocity maps. *Geophysical Journal International*, 173(1):281.
- [11] Maranó, S. and Fäh, D. (2014). Processing of translational and rotational motions of surface waves: Performance analysis and applications to single sensor and to array measurements. *Geophysical Journal International*, 196:317–339.
- [12] Matichard, F. et al. (2015). Seismic isolation of advanced ligo: Review of strategy, instrumentation and performance. *Classical and Quantum Gravity*, 32(18):185003.
- [13] Meier, T., Dietrich, K., Stöckhert, B., and Harjes, H. (2004). One-dimensional models of shear wave velocity for the eastern mediterranean obtained from the inversion of rayleigh wave phase velocities and tectonic implications. *Geophysical Journal International*, 156(1):45–58.
- [14] Pancha, A., Webb, T. H., Stedman, G. E., McLeod, D. P., and Schreiber, K. U. (2000). Ring laser detection of rotations from teleseismic waves. *Geophysical Research Letters*, 27(21):3553–3556.
- [15] Reinwald, M., Bernauer, M., Igel, H., and Donner, S. (2016). Improved finite-source inversion through joint measurements of rotational and translational ground motions: a numerical study. *Solid Earth*, 7(5):1467–1477.
- [16] Venkateswara, K., Hagedorn, C. A., Gundlach, J. H., Kissel, J., Warner, J., Radkins, H., Shaffer, T., Lantz, B., Mittleman, R., Matichard, F., and Schofield, R. (2017). Subtracting tilt from a horizontal seismometer using a ground rotation sensor. *Bulletin of the Seismological Society of America*, 107(2):709–717.

- [17] Venkateswara, K., Hagedorn, C. A., Turner, M. D., Arp, T., and Gundlach, J. H. (2014). A high-precision mechanical absolute-rotation sensor. *Review of Scientific Instruments*, 85(1).

BIBLIOGRAPHY

- [1] Aasi, J. et al. (2015). Advanced ligo. *Classical and Quantum Gravity*, 32(7):074001.
- [2] B Arp, T., A Hagedorn, C., Schlamming, S., and H Gundlach, J. (2013). A reference-beam autocollimator with nanoradian sensitivity from mhz to khz and dynamic range of 10(7.). *The Review of scientific instruments*, 84:095007.
- [3] Belfi, J., Beverini, N., Carelli, G., Di Virgilio, A., Maccioni, E., Saccorotti, G., Stefani, F., and Velikoseltsev, A. (2012). Horizontal rotation signals detected by “g-pisa” ring laser for the mw = 9.0, march 2011, japan earthquake. *Journal of Seismology*, 16(4):767–776.
- [4] et. al., S. (2016). First deep underground observation of rotational signals from an earthquake at teleseismic distance using a large ring laser gyroscope. *arXiv*.
- [5] Haskell, N. A. (1953). The dispersion of surface waves on multilayered media. *Bulletin of the Seismological Society of America*, 43(1):17–34.
- [6] Lantz, B., Schofield, R., O’Reilly, B., Clark, D. E., and DeBra, D. (2009). Review: Requirements for a ground rotation sensor to improve advanced ligo. *Bulletin of the Seismological Society of America*, 99(2B):980–989.
- [7] Lee, W. H. K., Celebi, M., Todorovska, M. I., and Igel, H. (2009). Introduction to the special issue on rotational seismology and engineering applications. *Bulletin of the Seismological Society of America*, 99(2B):945–957.
- [8] Legendre, C. P., Zhao, L., Huang, W.-G., and Huang, B.-S. (2015). Anisotropic rayleigh-wave phase velocities beneath northern vietnam. *Earth, Planets and Space*, 67(1):28.

- [9] Lin, C.-J., Huang, H.-P., Pham, N. D., Liu, C.-C., Chi, W.-C., and Lee, W. H. K. (2011). Rotational motions for teleseismic surface waves. *Geophysical Research Letters*, 38(15):n/a–n/a. L15301.
- [10] Lin, F.-C., Moschetti, M. P., and Ritzwoller, M. H. (2008). Surface wave tomography of the western united states from ambient seismic noise: Rayleigh and love wave phase velocity maps. *Geophysical Journal International*, 173(1):281.
- [11] Maranó, S. and Fäh, D. (2014). Processing of translational and rotational motions of surface waves: Performance analysis and applications to single sensor and to array measurements. *Geophysical Journal International*, 196:317–339.
- [12] Matichard, F. et al. (2015). Seismic isolation of advanced ligo: Review of strategy, instrumentation and performance. *Classical and Quantum Gravity*, 32(18):185003.
- [13] Meier, T., Dietrich, K., Stöckhert, B., and Harjes, H. (2004). One-dimensional models of shear wave velocity for the eastern mediterranean obtained from the inversion of rayleigh wave phase velocities and tectonic implications. *Geophysical Journal International*, 156(1):45–58.
- [14] Pancha, A., Webb, T. H., Stedman, G. E., McLeod, D. P., and Schreiber, K. U. (2000). Ring laser detection of rotations from teleseismic waves. *Geophysical Research Letters*, 27(21):3553–3556.
- [15] Reinwald, M., Bernauer, M., Igel, H., and Donner, S. (2016). Improved finite-source inversion through joint measurements of rotational and translational ground motions: a numerical study. *Solid Earth*, 7(5):1467–1477.
- [16] Venkateswara, K., Hagedorn, C. A., Gundlach, J. H., Kissel, J., Warner, J., Radkins, H., Shaffer, T., Lantz, B., Mittleman, R., Matichard, F., and Schofield, R. (2017). Subtracting tilt from a horizontal seismometer using a ground rotation sensor. *Bulletin of the Seismological Society of America*, 107(2):709–717.

- [17] Venkateswara, K., Hagedorn, C. A., Turner, M. D., Arp, T., and Gundlach, J. H. (2014). A high-precision mechanical absolute-rotation sensor. *Review of Scientific Instruments*, 85(1).